A fast time-difference inverse solver for 3D EIT with application to lung imaging

Ashkan Javaherian[1], Manuchehr Soleimani[2], Knut Moeller[1]

[1]Institute of Technical Medicine, Faculty of Medical and Life Sciences, Furtwangen University of Applied Sciences, VS-Schwenningen, Germany

[2]Engineering Tomography Laboratory (ETL), Department of Electrical Engineering, University of Bath, Bath, UK

E-mail: m.soleimani@bath.ac.uk

Abstract- A class of sparse optimization techniques that require solely matrix-vector products, rather than an explicit access to the forward matrix and its transpose, has been paid much attention in the recent decade for dealing with large-scale inverse problems. This study tailors application of the so-called Gradient Projection for Sparse Reconstruction (GPSR) to large-scale time-difference three-dimensional electrical impedance tomography (3D EIT). 3D EIT typically suffers from the need for a large number of voxels to cover the whole domain, so its application to real-time imaging, for example monitoring of lung function, remains scarce since the large number of degrees of freedom of the problem extremely increases storage space and reconstruction time. This study shows the great potential of the GPSR for large-size time-difference 3D EIT. Further studies are needed to improve its accuracy for imaging small-size anomalies.

Keywords: three-dimensional electrical impedance tomography, sparse recovery, Gradient Projection for Sparse Reconstruction, lung imaging

1. Introduction

Electrical Impedance Tomography (EIT) is a diffusive imaging modality for reconstructing the conductivity field inside an object from surface electrical measurements [1,2]. This technique has many applications in medicine, e.g., real-time monitoring of lung [3,4], detection of breast tumors [5], or imaging of brain activity [6]. Typically, a number of electrodes are attached to the skin of the subject, a small alternating current is injected through some of these electrodes successively, and the induced electrical potentials are measured on the remaining electrodes [1,2].

The image reconstruction is done by iteratively updating the conductivity field until ℓ_2 norm of discrepancy between simulated and real measured data is minimized. From a theoretical point of view, it involves alternatively a nonlinear forward problem of calculating the surface voltages from the conductivity field via finite element method (FEM) and a severely ill-posed inverse problem for updating the conductivity field from the surface voltages [7-9]. To cope with the nonlinear

relationship between the conductivity field and the data sets, a Jacobian (sensitivity) matrix is computed to linearize the problem around a homogenous conductivity [8,9]. To deal with the high ill-posedness of the problem, the inverse problem is often regularized via assuming *a priori* assumptions about the conductivity field [10-12].

EIT is an efficient tool for real-time monitoring of lung since there is a large contrast between the conductivity of air and that of the encompassing tissues [4]. There are, however, some sources of error during the measurement. Breathing action or posture changes may move the electrodes during the measurements, thus deleteriously affecting the recovered conductivity [13,14]. To cope with such errors, time-difference reconstruction is often given precedence over absolute reconstruction. Employing the time-difference reconstruction, the objective is to infer conductivity changes from difference between two boundary data sets that are measured at different times [14].

Classical quadratic inverse solvers in EIT often consider some correlations between adjacent finite elements, thereby reducing the ill-posedness of the problem [11]. In this way, the problem is stabilized at the cost of imposing some smoothness on the reconstructed image, so detecting sharp discontinuities over the conductivity field will be impossible [15,16]. There are, however, many organs that have well defined boundaries, and thus represent sharp variations over the conductivity profile, e.g., interfaces between collapsed and ventilated regions of lung [15, 17].

To overcome this effect, Total variation (TV) regularization has been applied to EIT, thanks to its ability to better preserve sharp interfaces, compared to the classical quadratic regularization [15,18]. To the best of our knowledge, the TV reconstruction schemes that have been applied to EIT so far are based on Newton's method, e.g., Primal-Dual interior point method or Lagged diffusivity method [15,18]. These codes are available on EIDORS website [19]. Newton's methods intuitively require inverse Hessian, so their application to 3D EIT leads to very large computations.

EIT is inherently three dimensional since electrical current cannot be confined to flow solely at the electrodes plane. As a result, 2D EIT is subject to artefacts produced by contrasts that are off the electrodes plane [20]. 3D EIT has thus received much attention with at least two planes of electrodes [20-30]. Among quadratic regularized solvers, Krylov subspace methods such as Conjugate Gradient (CG) best suit 3D EIT, as classical Newton's methods involve the costly inversion of Hessian [26-28]. Indeed, the very large size of forward operator in 3D EIT increases the ill-posedness of the problem, as well as computational time. As a result, the main advantage of EIT over other imaging modalities for real time imaging will be lost [29,30].

Finding sparse solutions to large-size linear systems of equations has attracted much interest recently [31-33]. The presence of an ℓ_1 norm as the regularization function encourages small components of the unknown parameters to become exactly zero, thus promoting sparse solutions [31].

To reduce the computational cost of calculating the conductivity over a large number of finite elements in 3D EIT, this study tailors the application of a class of sparsity inverse solvers that does not require the Jacobian ($\mathbf{J}$) to be stored explicitly, but only needs matrix-vector products including $\mathbf{J}$ and $\mathbf{J}^T$ [31-34]. This study shows the great potential of the so-called Gradient Projection for Sparse Reconstruction (GPSR) method for time-difference 3D EIT. The GPSR was first proposed in the context of signal processing [31], and has then been extended to other applications (See [35-42]). Applying time-difference imaging, the GPSR splits the update at each iterate into its negative and positive parts, and then enforces a nonnegativity constraint on each part so that the background conductivity is gradually set to zero with the progress of the solver [31]. Since for the time-difference reconstruction, the background is typically set to zero, and a solution around zero is expected, it benefits notably from the splitting behavior of the GPSR, unlike other competing sparsity solvers, which fail to possess this advantage.

Furthermore, the superiority of the GPSR over other popular sparsity solvers, e.g., l1-ls [32], two-step iterative shrinkage thresholding (TWIST) [33], or fixed-point continuation (FPC) [34], for large-scale inverse problems has already been demonstrated, e.g. [31].

The sparsity regularization for EIT has attracted much interest recently. To best of our knowledge, the most well-known algorithm for sparsity reconstruction in EIT was proposed in [43], and was then applied to real experiments [44,45]. Although similar to the GPSR, this algorithm follows a gradient-based method which requires solely matrix-vector products, it does not benefit from the splitting scheme in the GPSR. In addition, a direct application of the Gradient of the residual leads to numerical instability for this algorithm, even in two-dimensional cases, so a Sobolev smoothing step is applied to the gradient via solving an augmented Dirichlet boundary value problem at each iterate, which increases the computational cost [43-45].

Typically, the gradient-based sparsity reconstruction considerably reduces the computational cost in comparison to Newton-based ℓ_1 reconstructions such as [46]. In spite of the very fast nature of these solvers, which is highly demanded for 3D imaging of lung function, their application to 3D lung imaging has not been reported so far. To the best of our knowledge, this manuscript reports the first application of the Gradient-based sparsity reconstruction for this case.

Preconditioned Conjugate Gradient (PCG), the most popular algorithm for large-size 3D EIT, available on the EIDORS website [19], is considered as the first benchmark [26-28]. The second benchmark is the sparsity algorithm specified for EIT in [43-45].

2. Method

2.1. Forward and inverse models

The forward problem in EIT is to calculate the surface electrical potentials on the electrodes ($\mathbf{U}$) as a function of the injected currents ($\mathbf{I}$) and the conductivity distribution ($\boldsymbol{\sigma}$). To implement the forward problem, elliptic partial differential equations (PDEs) are defined over the mesh according to Ohm's law. Neumann and Dirichlet boundary conditions are determined as functions of the boundary data sets ($\mathbf{I}, \mathbf{U}$). The resulting nonlinear systems of equations are written as $\mathbf{U} = \gamma F(\boldsymbol{\sigma})\mathbf{I}$, where $F(\boldsymbol{\sigma}): \mathbf{I} \to \mathbf{u}$ denotes Neumann-to-Dirichlet (NtD) map, and $\gamma: \mathbf{u} \to \mathbf{U}$ represents Dirichlet-to-observation map [1,2]. The resulting problem is nonlinear with respect to the conductivity, so it is linearized around the background conductivity $\boldsymbol{\sigma}^{bg}$ via computing the Jacobian ($\mathbf{J}$) as follows [9].

$$\delta\mathbf{U} = \gamma(F(\boldsymbol{\sigma}) - F(\boldsymbol{\sigma}^{bg}))\mathbf{I} \approx \mathbf{J}(\boldsymbol{\sigma} - \boldsymbol{\sigma}^{bg}). \tag{1}$$

Applying the time-difference imaging, the objective is to calculate conductivity changes $\delta\boldsymbol{\sigma}$ from difference between two data frames that are measured at times t_1 and t_2 ($\delta\mathbf{V}$) [13,14]. In a matrix notation, in light of $\delta\mathbf{U} = \mathbf{J}\delta\boldsymbol{\sigma}$, the inverse problem is to infer $\delta\boldsymbol{\sigma}$ from the real difference measured data $\delta\mathbf{V}$ in the form

$$\min_{\delta\boldsymbol{\sigma}} \quad \left\|\mathbf{J}\delta\boldsymbol{\sigma} - \delta\mathbf{V}\right\|_2^2 \quad \text{s.t.} \quad \text{a priori assumption on } \delta\boldsymbol{\sigma} \tag{2}$$

The unconstrained Tikhonov form of (2) can be written as

$$\min_{\delta\boldsymbol{\sigma}} \quad \left\|\mathbf{J}\delta\boldsymbol{\sigma} - \delta\mathbf{V}\right\|_2^2 + \lambda R_r(\delta\boldsymbol{\sigma}), \tag{3}$$

where

$$R_r(\vartheta) = \frac{1}{r}\left\|\vartheta\right\|_{\ell_r}^r. \tag{4}$$

2.2. Preconditioned Conjugate Gradient (PCG) inverse solver

The choice of $r = 2$ turns problem (3) to quadratic regularized form [8-12]. In this work, to evade the costly computation of inverse Hessian, the quadratic optimization problem is solved by the PCG, rather than Newton's methods. PCG method is a Krylov subspace techniques [47]. Generally, setting the derivative of least squares problem $\min_{\delta\boldsymbol{\sigma}}\left\|\delta\mathbf{V} - \mathbf{J}\delta\boldsymbol{\sigma}\right\|_2^2$ to zero yields

$$\mathbf{J}^T\mathbf{J}\delta\boldsymbol{\sigma} = \mathbf{J}^T\delta\mathbf{V}. \tag{5}$$

Applying the PCG to Eq. (5) yields the following optimization algorithm. Given $\mathbf{J}$, $\delta\mathbf{V}$, initial guess $\delta\boldsymbol{\sigma}_0$, preconditioner $\mathbf{M}$, and stopping tolerance ε, the algorithm is outlined as follows.

Algorithm 1. Preconditioned Conjugate Gradient [47]

$\delta\boldsymbol{\sigma}^0 = 0$

$\mathbf{r}^0 = \delta\mathbf{V} - \mathbf{J}\delta\boldsymbol{\sigma}^0$

$\mathbf{d}^0 = \mathbf{M}^{-1}\mathbf{r}^0$

$\tau^0 = (\mathbf{r}^0)^T\mathbf{d}^0$

While $(\tau^k / \tau^0) > \varepsilon$ **Do**

$\mathbf{q}^k = \mathbf{J}\mathbf{d}^k$

$$\alpha^k = \frac{\tau^{k-1}}{(\mathbf{d}^k)^T\mathbf{q}^k}$$

$\delta\boldsymbol{\sigma}^k \leftarrow \delta\boldsymbol{\sigma}^{k-1} + \alpha^k\mathbf{d}^k$

$\mathbf{r}^k \leftarrow \mathbf{r}^{k-1} - \alpha^k\mathbf{q}^k$

$\mathbf{s}^k = \mathbf{M}^{-1}\mathbf{r}^k$

$\tau^k = (\mathbf{r}^k)^T\mathbf{s}^k$

$$\beta^k = \frac{\tau^k}{\tau^{k-1}}$$

$\mathbf{d}^{k+1} \leftarrow \mathbf{s}^k + \beta^k\mathbf{d}^k$

$k \leftarrow k + 1$

End Do

Where, d^k and α^k denote the search direction and step length at iteration k, respectively. In this work, the PCG is implemented with the aid of the EIDORS software [19], and is regarded as the first benchmark for evaluating the performance of the proposed inverse solver. The second benchmark is the most well-known sparsity algorithm in EIT [43-45], which is outlined in appendix. For further theoretical details, the reader is referred to [43-45].

2.3. Sparse recovery

Many different approaches have been proposed to seek a sparse solution to large-size linear system $\mathbf{y} = \mathbf{A}\mathbf{x} + \mathbf{n}$, where $\mathbf{y}$ is the observation data and $\mathbf{n}$ is the noise. Roughly they can be divided into two

categories, i.e., constrained and unconstrained optimization problems. Assuming T and ε to be nonnegative parameters, the constrained form leads to the following two formulations, i.e.,

$$\min_{\mathbf{x}} \quad \|\mathbf{y}-\mathbf{A}\mathbf{x}\|_2^2 \quad \text{s.t.} \quad \|\mathbf{x}\|_1 \le T, \tag{6}$$

the so-called *Quadratic program (QP)*, i.e., *least absolute shrinkage and selection operator* (LASSO) [48], and

$$\min_{\mathbf{x}} \quad \|\mathbf{x}\|_1 \quad \text{s.t.} \quad \|\mathbf{y}-\mathbf{A}\mathbf{x}\|_2^2 \le \varepsilon, \tag{7}$$

namely *Quadratically constrained linear program (QCLP)*, or *Basis pursuit* with $\varepsilon = 0$ [49].

There has also been much interest in solving the unconstrained form of the problem, i.e.,

$$\min_{\mathbf{x}} \quad \|\mathbf{y}-\mathbf{A}\mathbf{x}\|_2^2 + \lambda\|\mathbf{x}\|_1, \tag{8}$$

where λ is the regularization parameter. It was proved that a solution of (6) for $T \ge 0$ is a minimizer of (8) for some $\lambda > 0$. Similarly, a solution of (7) is either $\boldsymbol{X} = 0$, or a minimizer of (8) for some $\lambda > 0$ (31).

2.4. Gradient Projection for Sparse Reconstruction (GPSR) inverse solver

The choice of $r = 1$ conducts problem (3) to

$$\min_{\delta\boldsymbol{\sigma}} \quad \|\delta\mathbf{V}-\mathbf{J}\delta\boldsymbol{\sigma}\|_2 + \lambda\|\delta\boldsymbol{\sigma}\|_1, \tag{9}$$

which is equivalent to Eq. (8).

The GPSR approach is applied in this work to infer a sparse solution of the conductivity changes from the difference data $\delta\boldsymbol{V}$. The base of this approach is to initially split the unknown vector $\delta\boldsymbol{\sigma}$ into its positive and negative parts, and then enforcing a nonnegativity constraint on each part [31], i.e.,

$$\delta\boldsymbol{\sigma} = \mathbf{u}-\mathbf{w}, \quad \mathbf{u} \ge 0, \mathbf{w} \ge 0. \tag{10}$$

Accordingly, considering a mesh made up of n finite elements, for $i = 1,2,...,n$,

$$\begin{aligned} \mathbf{u}_i &= (\delta\boldsymbol{\sigma}_i)_+ \\ \mathbf{w}_i &= (-\delta\boldsymbol{\sigma}_i)_+, \end{aligned} \tag{11}$$

where $(x)_+ = \max\{0, x\}$. Considering the penalty term in (9) in the form $\|\delta\boldsymbol{\sigma}\|_1 = \mathbf{1}_n^T\mathbf{u} + \mathbf{1}_n^T\mathbf{w}$ with $\mathbf{1}_n = [1,1,...,1]^T$ yields [31]

$$\min_{\mathbf{u},\mathbf{w}} \ \|\delta\mathbf{V} - \mathbf{J}(\mathbf{u}-\mathbf{w})\|_2^2 + \lambda\mathbf{1}_n^T\mathbf{u} + \lambda\mathbf{1}_n^T\mathbf{w} \quad \text{s.t.} \quad \mathbf{u} \geq 0, \mathbf{w} \geq 0 \ . \tag{12}$$

Supposing $\mathbf{z} = \begin{bmatrix}\mathbf{u}\\ \mathbf{w}\end{bmatrix}$, $\mathbf{c} = \lambda\mathbf{1}_{2n} + \begin{bmatrix}-\mathbf{J}^T\delta\mathbf{V}\\ \mathbf{J}^T\delta\mathbf{V}\end{bmatrix}$ and $\mathbf{B} = \begin{bmatrix}\mathbf{J}^T\mathbf{J} & -\mathbf{J}^T\mathbf{J}\\ -\mathbf{J}^T\mathbf{J} & \mathbf{J}^T\mathbf{J}\end{bmatrix}$, (12) is rewritten as

$$\min_{\mathbf{z}} \ \mathbf{c}^T\mathbf{z} + \frac{1}{2}\mathbf{z}^T\mathbf{B}\mathbf{z} \equiv \phi(\mathbf{z}) \quad \text{s.t.} \quad \mathbf{z} \geq 0. \tag{13}$$

Now Gradient projection (GP) method is employed, which involves two stages at each iteration [31,50]. First, given $\mathbf{z}^k$, $\alpha^k > 0$ is chosen as a step length for searching along negative direction $-\nabla\phi(\mathbf{z}^k)$ from $\mathbf{z}^k$ in the feasible set.

$$\boldsymbol{\theta}^k = (\mathbf{z}^k - \alpha^k\nabla\phi(\mathbf{z}^k))_+ \tag{14}$$

The nonnegativity constraint imposed to $\boldsymbol{\theta}^k$ iteratively nulls the background with the progress of the algorithm. $\tau^k \in [0,1]$ is then chosen to set

$$\mathbf{z}^{k+1} = \mathbf{z}^k + \tau^k(\boldsymbol{\theta}^k - \mathbf{z}^k). \tag{15}$$

The step length α^k is chosen in two different ways, which is explained in the sequel.

2.4.1. Basic GPSR

Employing the basic variant of the GPSR, the gradient is defined as [31]

$$\mathbf{g}_i^k = \begin{cases}\nabla\phi(\mathbf{z}^k)_i, & \text{if} \quad \mathbf{z}_i^k > 0 \quad \text{or} \quad (\nabla\phi(\mathbf{z}^k))_i < 0\\ 0, & \text{otherwise}\end{cases}, \tag{16}$$

Applying the gradient in this way prevents the elements of $\mathbf{z}$ that were nulled by the constraint in the previous iterates from any further updates, reducing the number of degrees of freedom of the problem iteratively. An initial guess for α is chosen so that ϕ is minimized along $\mathbf{g}^k$, i.e.,

$$\alpha_0^k = \arg\min_{\alpha} \phi(\mathbf{z}^k - \alpha\mathbf{g}^k). \tag{17}$$

An exact minimizer for the above problem is written as [31]

$$\alpha_0^k = \frac{(\mathbf{g}^k)^T \mathbf{g}^k}{(\mathbf{g}^k)^T \mathbf{B}\mathbf{g}^k}, \tag{18}$$

α^0 is then encountered by upper and lower bounds $\alpha_{\min}$ and $\alpha_{\max}$. For the backtracking line search, considering scalar parameters $\beta \in (0,1)$ and $\mu \in (0,1/2)$, α^k is chosen to be the first value in the sequence $\alpha^0, \beta\alpha^0, \beta^2\alpha^0, \ldots$ that satisfies

$$\phi((\mathbf{z}^k - \alpha^k \nabla\phi(\mathbf{z}^k))_+) \le \phi(\mathbf{z}^k) - \mu\nabla\phi(\mathbf{z}^k)^T(\mathbf{z}^k - (\mathbf{z}^k - \alpha^k\nabla\phi(\mathbf{z}^k))_+) \tag{19}$$

2.4.2. Barzilai-Borwein GPSR

Employing Barzilai-Borwein (BB) scheme, α^k is chosen such that $\alpha^k I$ approaches the inverse Hessian $\nabla^2\phi(x)$ over the latest step. Letting $s^k = \mathbf{z}^k - \mathbf{z}^{k-1}$ and $v^k = \nabla\phi(\mathbf{z}^k) - \nabla\phi(\mathbf{z}^{k-1})$, the exact step length is computed as

$$\alpha_0^k = \arg\min_{\alpha} \left\| \alpha s^k - v^k \right\|_2^2 = \frac{(s^k)^T v^k}{(s^k)^T s^k}. \tag{20}$$

α^0 is then encountered by upper and lower bounds $\alpha_{\min}$ and $\alpha_{\max}$, similar to the basic GPSR. In comparison to the BB GPSR in [31], a more sophisticated version of the BB rule was employed in our study. This BB rule was similarly applied to the standard sparsity algorithm presented in Appendix, according to [43-45]. The step length computed by Eq. (20) is reduced in an inner iteration by a constant factor until the following criterion in Eq. (21) is satisfied. It turns out that enforcing monotonicity would deteriorate the behavior of the BB rule on the convergence. As a result, a globally convergent Barzilai-Borwein is employed, where $\mathbf{z}^{k+1}$ is accepted as a new iterate if [52]

$$\Phi(\mathbf{z}^{k+1}) \le \max_{(k-Q+1 \le i \le k)} \Phi(z^i) - \alpha^k \frac{\mu}{2} \left\| \mathbf{z}^{k+1} - \mathbf{z}^k \right\|_2^2. \tag{21}$$

Where i denotes the Q previous iterations, and $\mu \in (0,1)$ is a constant that is often chosen near zero. The stopping criterion is defined based on perturbation results for linear complementarity problems (LCP) as follows [31,53]. There exists a scalar parameter ξ such that

$$\mathrm{dist}(\mathbf{z}, \mathbf{s}) \le \xi \left\| \min(\mathbf{z}, \nabla\phi(\mathbf{z}) \right\|, \tag{22}$$

where $\mathbf{s}$ represents the solution to problem (13), $\mathrm{dist}(\cdot)$ denotes the distance operator, and the minimizing operator is taken component-wise. In light of (22), the algorithm is terminated if

$$\left\|\min(\mathbf{z}, \nabla\phi(\mathbf{z})\right\| \le tol. \tag{23}$$

The GPSR algorithm is outlined as follows.

Algorithm 2. Gradient Projection for Sparse Reconstruction [31]

Set $\mathbf{z}^0 = 0$, and choose $\alpha^0 \in [\alpha_{\min}, \alpha_{\max}]$

While stopping criterion is not satisfied **Do**

Choose α^k based on basic (2.4.1) or BB (2.4.2) scheme

Set $\boldsymbol{\rho}^k = (\mathbf{z}^k - \alpha^k \nabla\phi(\mathbf{z}^k))_+ - \mathbf{z}^k$

Calculate $\tau^k = \text{mid}\left\{0, \frac{(\boldsymbol{\rho}^k)^T \nabla\phi(\mathbf{z}^k)}{(\boldsymbol{\rho}^k)^T \mathbf{B}\boldsymbol{\rho}^k}, 1\right\}$

Set $\mathbf{z}^{k+1} = \mathbf{z}^k + \tau^k \boldsymbol{\rho}^k$

$k \leftarrow k + 1$

End Do

2.5. Analysis of computational cost

At first glance, the problem (13) may appear more costly than the classical form of the problem in (12) since the dimension of the problem becomes twice, i.e., $\mathbf{z} \in R^{2n}$. However, Considering $\phi(\mathbf{z}) = \mathbf{c}^T\mathbf{z} + \frac{1}{2}\mathbf{z}^T\mathbf{B}\mathbf{z}$, matrix $\mathbf{c} = \lambda \mathbf{1}_{2n} + \begin{bmatrix} -\mathbf{J}^T\delta\mathbf{V} \\ \mathbf{J}^T\delta\mathbf{V} \end{bmatrix}$ is independent from the unknown parameter $\delta\boldsymbol{\sigma}$, so it can be computed once at the start of the algorithm. In addition, $\mathbf{z}^T\mathbf{B}\mathbf{z}$ yields a scalar value, which can be easily calculated as

$$\mathbf{z}^T\mathbf{B}\mathbf{z} = (\mathbf{u}-\mathbf{w})^T\mathbf{J}^T\mathbf{J}(\mathbf{u}-\mathbf{w}) = \left\|\mathbf{J}(\mathbf{u}-\mathbf{w})\right\|_2^2. \tag{24}$$

Therefore, the total cost for the calculation of $\phi(\mathbf{z})$ at each iteration involves a matrix-vector product $\mathbf{J}(\mathbf{u}-\mathbf{w})$ and a vector-vector product $\mathbf{c}^T\mathbf{z}$. To minimize ϕ in problem (13), the gradient of $\phi(\mathbf{z})$ is computed at each iterate in the form

$$\nabla\phi(\mathbf{z}) = \mathbf{c} + \mathbf{B}\mathbf{z}. \tag{25}$$

Considering

$$\mathbf{B}\mathbf{z} = \begin{bmatrix} \mathbf{J}^T\mathbf{J}(\mathbf{u}-\mathbf{w}) \\ -\mathbf{J}^T\mathbf{J}(\mathbf{u}-\mathbf{w}) \end{bmatrix}, \tag{26}$$

the cost for computing $\nabla\phi(\mathbf{z})$ is two matrix-vector products, as $\mathbf{c}$ is calculated independently from the iterates. In this study, the application of the GPSR to 3D EIT was tailored. To implement the GPSR, a MATLAB code in the context of signal processing, which is available online [54], was modified.

3. Numerical results

A 3D shape of an adult human thorax was simulated by using the EIDORS and NETGEN software as follows [19,55]. The contour of a human thorax and lungs were plotted according to a CT image available on the EIDORS, and were then mapped onto a 3D finite element mesh generated by the NETGEN software [55]. The created 3D mesh was made up of 161021 tetrahedral elements with a height of 1. Thirty two circular electrodes were installed around the chest in two rings aligned by axial planes 0.33 and 0.66. The electrodes were simulated based on complete electrode model with a contact impedance of 100 Ω and a radius of 0.05 [23]. An electrical current with amplitude of 5 mA was successively injected through the electrodes, and the induced potentials were measured according to planar alignment protocol, the most well-known protocol for 3D EIT [20].

The noise contributed to the measurement data was an additive white Gaussian noise (AWGN). Considering the difference imaging, AWGN is simulated as

$$\text{Noise} = NL \times std(\delta V) \times randn, \tag{27}$$

where, where *NL* is noise level, *std* is standard deviation of difference between two frames of data, and *randn* is a vector denoting pseudorandom values drawn over a standard Gaussian distribution. The simulated data was contaminated with a 20 db AWGN, i.e., $NL = 10^{-20/20} = 0.1$ (see [19]).

To avoid the so-called inverse crime, the inverse solver was applied to a coarser mesh made up of 20955 elements. The background conductivity was set to 1, while the lungs' conductivity was set to $0.3\,\mathrm{Sm}^{-1}$. Fig. 1(a) shows the simulated chest phantom from a 3D view. Figs. 1(b) and (c), respectively, exhibit the mesh from a top and a lateral view. The time-difference reconstruction was employed with the background conductivity as the reference data.

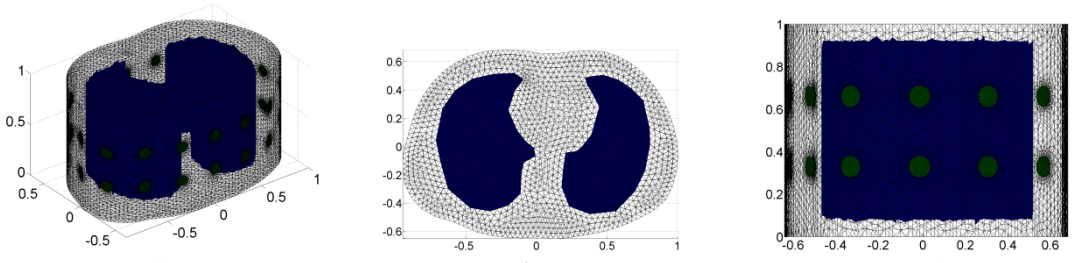

(a) (b) (c)

Fig. 1. The simulated human chest from: (a) a 3D view, (b) a top view, and (c) a lateral view.

The PCG solver was implemented, and terminated at threshold $\varepsilon = 1e-2$. This parameter was heuristically selected to produce the image best fitting the simulated model over 100 iterates. The sparsity algorithm specified for EIT in [43-45], referred to as ''*standard sparsity algorithm''* here, the basic GPSR and BB GPSR were implemented, and were continued until the threshold $tol = 1e-2$. Heuristically, among a wide range of regularization parameters, $\lambda = 1e-4$ produced the optimal image for both the basic and BB GPSR. The optimal image for the standard sparsity algorithm was produced by $\lambda = 5e-7$.

Fig. 2 displays the 3D images reconstructed by the solvers at equidistant axial cross sections. From the left side, the first column corresponds to the 3D image reconstructed by the PCG solver, the second column represents the standard sparsity algorithm, and the third and fourth columns pertain to the basic GPSR, and BB GPSR, respectively. The slices were exhibited according to the colourbar shown to the right of each column, which was adjusted such that its minimal value represents discrepancy of the conductivity between the lungs and background in the simulated phantom, i.e., -0.7 Sm^{-1}. The vertical position of each transverse plane was written to the left of the figure.

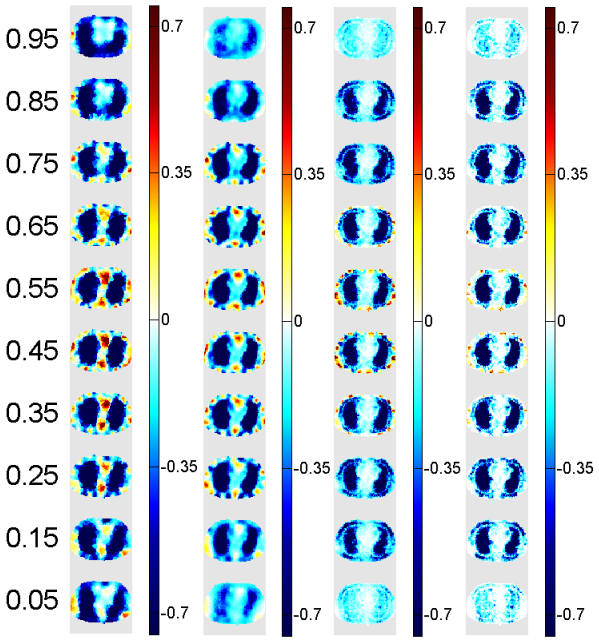

Fig. 2. From the left side, the 3D images reconstructed by the PCG, standard sparsity, basic GPSR, and BB GPSR, displayed at transverse planes written to the left of the figure.

Observations. As shown in the left column of Fig. 2, the PCG produced a great blurriness, and failed to precisely detect the sharp conductivity jumps over the reconstructed image. These smoothing effects have given rise to a low spatial resolution aligning all dimensions. A fair comparison between Fig. 1 (b) and the second column in Fig. 2 reveals that the standard sparsity algorithm was not tolerant enough to accurately determine the lung boundaries. Furthermore, comparing the second column to

Fig. 1(c) shows that the spatial resolution aligning the longitudinal axis has been lost, and a great artefact has been produced in the top and bottom slices, where the lungs do not exist.

As displayed in the third and fourth columns of Fig. 2, the GPSR solver considerably improved the reconstruction in determining the sharp jumps over the conductivity profile. A comparison between Fig. 1 and the two last columns reveals that the GPSR determined the lung boundaries more accurately than the PCG and standard sparsity algorithms over all the transverse planes. According to the colourbars, the GPSR determined the conductivity changes amplitude with a much higher accuracy as well. Furthermore, compared to the basic GPSR, conducting the GPSR through the BB scheme improved the solution regarding contrast, as well as the amount of artifact. Figs. 3 (a), (b) and (c), respectively, exhibit the images reconstructed by the standard sparsity, basic GPSR and BB GPSR from a 3D view. In other words, Figs. 3(a), (b) and (c) represent 3D views of the images shown in the second, third and fourth columns in Fig. 2. The image reconstructed by the PCG was neglected, as it was covered by very large amount of artefacts around the lungs.

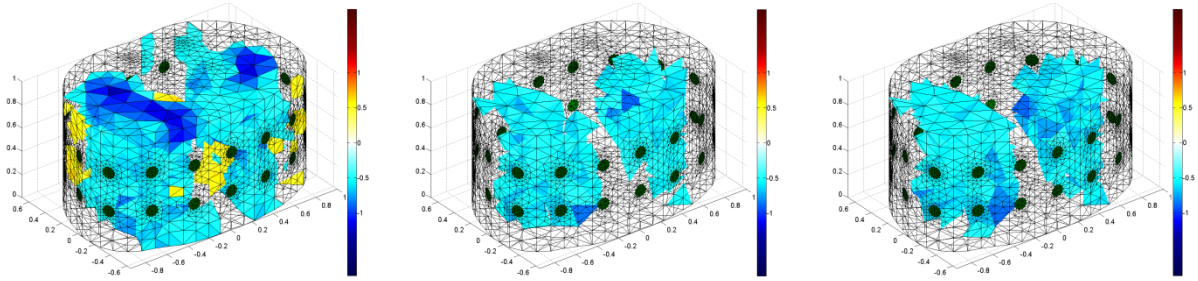

(a) (b) (c)

Fig. 3. The images reconstructed by: (a) the standard sparsity (second column in Fig. (2)), (b) basic GPSR (third column in Fig. (2)), and (c) BB GPSR (fourth column in Fig. (2)), from a 3D view. To better visualize the inclusions, maximal values of colourbars were increased, compared to Fig.2.

The performance of the solvers was evaluated in terms of Relative Error (*RE*), i.e.,

$$RE = \frac{\left\| \boldsymbol{\sigma}_{solution} - \boldsymbol{\sigma}_{phantom} \right\|_2}{\left\| \boldsymbol{\sigma}_{phantom} \right\|_2}, \tag{28}$$

where $\boldsymbol{\sigma}_{phantom}$ denotes the conductivity distribution over the simulated phantom, and $\boldsymbol{\sigma}_{solution}$ denotes the computed absolute conductivity, i.e., the calculated conductivity changes plus the background. Accordingly, the first row in Table 1 shows the RE for the reconstructed images. The RE of the images reconstructed by the basic and BB GPSR was, respectively, 31% and 43% smaller than that of the standard sparsity algorithm. The PCG produced much greater RE than all the employed sparsity algorithms.

Computational cost. The second row in Table 1 shows the CPU time elapsed on implementing the solvers. All the computed CPU times involve 0.81 Sec for computation of the Jacobian. The processor that was employed in this work is an Intel® Core ™ i3-3220 Processor (3.30 GHz) with a RAM of 4GB and a 64-bit operating system (Windows 7, Microsoft, Seattle, WA).

Table 1. The RE of the images reconstructed from the simulated chest and the CPU time.

	PCG	Standard Sparse	Basic GPSR	BB GPSR
RE	0.61	0.35	0.24	0.20
Time	25.81	10.73	1.93	5.79

According to Table 1, the GPSR considerably reduced the computational time, compared to the competing algorithms. Since the BB scheme typically conducts the solution without forcing the objective function to decrease monotonically through all the iterations, the CPU time elapsed on the BB GPSR was three times more than the basic GPSR. In this way, the BB scheme reconstructed the image with an RE 17% smaller than the basic GPSR.

4. Experimental results

To validate the proposed image reconstruction, the algorithms were also tested on a real data measured from a human chest. The data, which is available on the EIDORS website, pertains to thirty four frames of a breathing cycle of a human subject [56]. To recover the real shape of lungs in a 3D representation, a very fine mesh was needed. Accordingly, the inverse problem was applied to a simulated chest made up of 143119 voxels. Fig. 4 displays the created mesh from a 3D view. The electrodes were placed aligning axial plane 0.5, and were represented by the green circles.

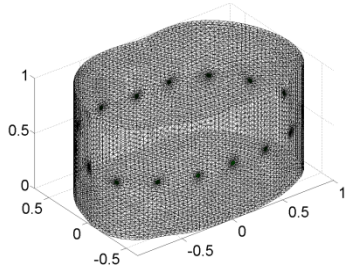

Fig. 4. The chest phantom created for reconstructing image from the experimental data pertaining to thirty four frames of a breathing cycle.

Employing the solvers, the time-difference imaging was applied such that the first frame was used as the reference data. The PCG algorithm was first employed, and the images were calculated at stopping threshold $\varepsilon = 7e-3$, which produced the best image heuristically. Fig. 5 shows the reconstructed images concerning all the thirty four frames. Note that these frames are originally 3D

images that are shown solely at axial plane 0.5, aligned by the electrodes plane, due to space constraints.

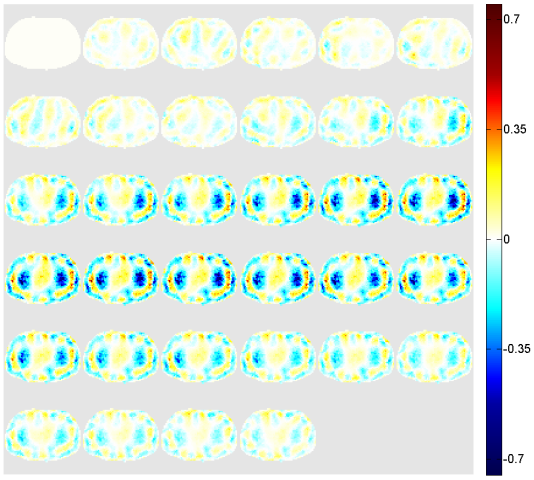

Fig. 5. The 3D images reconstructed by the PCG solver at thirty four frames of the breathing cycle. The slices were taken at the electrodes plane.

Since the simulated results showed the superiority of the GPSR over the standard sparsity algorithm proposed in [43-45] regarding both accuracy and time, the standard sparsity solver was neglected in this section. The GPSR solvers were implemented until $tol = 1e-2$, and 3D images were computed. The regularization parameter was heuristically chosen to be $\lambda = 1e-2$. Figs. 6(a) and (b), respectively, display the images reconstructed by the basic and BB GPSR at the electrodes plane.

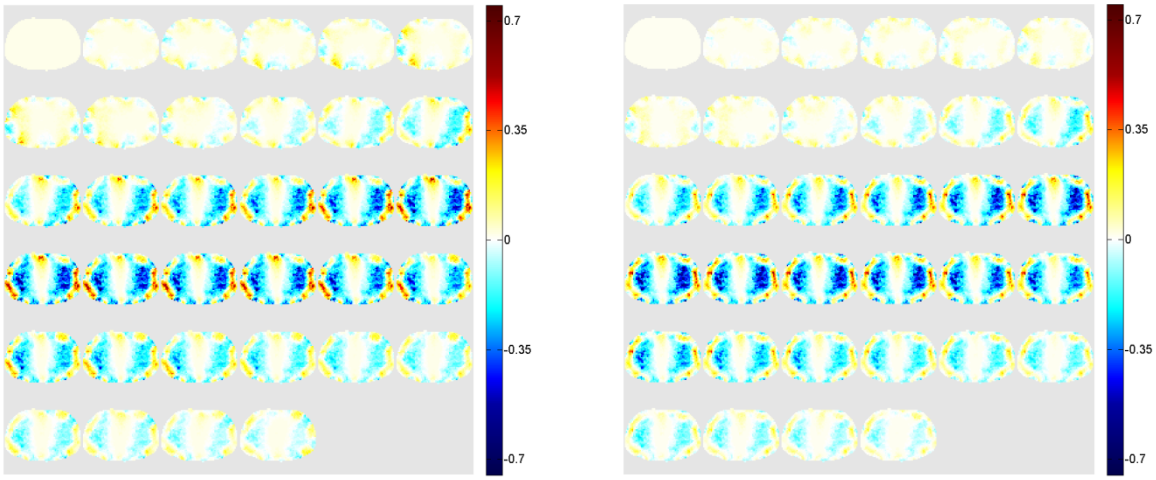

(a) (b)

Fig. 6. The 3D images reconstructed by: (a) the basic GPSR, and (b) BB GPSR at thirty four frames of the breathing cycle. The slices were taken at the electrodes plane.

Observations. The results show that PCG failed to accurately recover shape of the lungs over a 3D chest phantom with such large number of voxels. The images include great amounts of artifact as well. On the other hand, the GPSR considerably improved the reconstruction. Both the basic and BB GPSR better determine the lung shape during the breathing cycle, compared to the PCG. In addition, a fair comparison between Figs. 6(a) and (b) shows that the BB scheme provided a better contrast over the frames than the basic scheme, as well as a smaller amount of artefact.

For all the solvers, the maximal mean of conductivity changes occurred for the 22nd frame of the breathing cycle. Fig. 7 exhibits the images pertaining to the 14th, 22nd, and 30th frames from a 3D scene. Figs. 7(a), (b) and (c) show the images of the 14th frame, in the middle of inhalation stage, reconstructed by the PCG, basic and BB GPSR, respectively. Similarly, Figs. 7(d), (e) and (f) show 3D views of the images of the 22nd frame, maximum end-respiratory. Figs. 7(g), (h) and (i), respectively, represent the 3D images reconstructed by the PCG, basic and BB GPSR for the 30th frame of the breathing cycle, in the middle of exhalation stage. In other words, Figs. 7(a), (d) and (g) represent the three aforementioned frames of Fig. (5), Figs. 7(b), (e) and (h) show the 3D view of these frames in Fig. 6(a), and Figs. 7(c), (f) and (i) represent the corresponding frames of Fig. 6(b). To better visualize the 3D images, maximal values of colourbars were increased, compared to Figs. (5) and (6) so that very small artefacts were neglected. As shown in this figure, compared to the PCG, the GPSR solvers better recovered shape of the lungs, and reduced the amount of artefact.

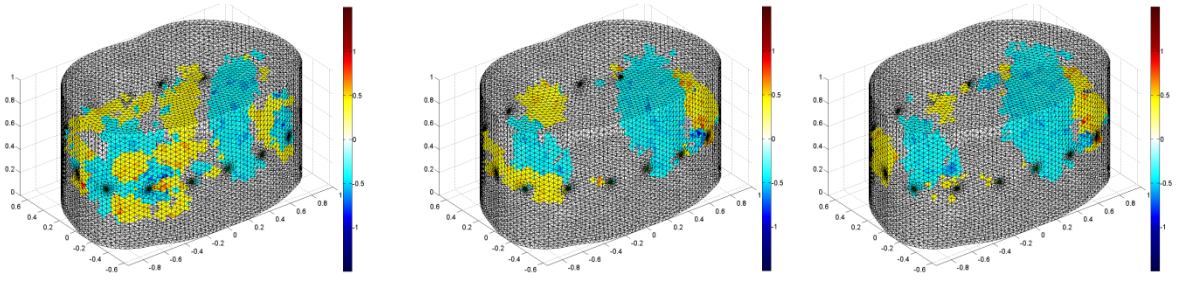

(a) (b) (c)

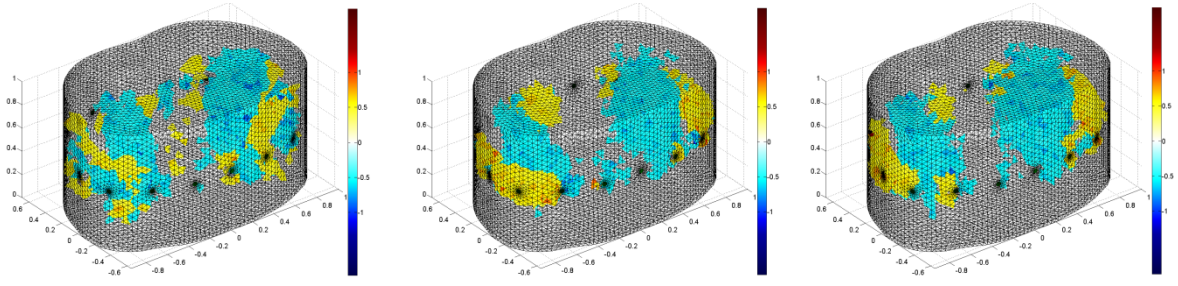

(d) (e) (f)

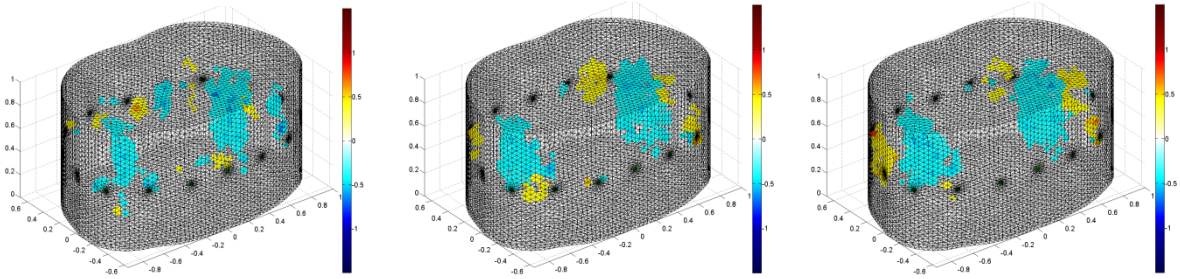

(g) (h) (i)

Fig. 7. The images of the 14th frame of the breathing cycle from a 3D view, reconstructed by: (a) PCG, (b) basic GPSR, and (c) BB GPSR, the images of the 22nd frame of the breathing cycle from a 3D view, reconstructed by: (d) PCG, (e) basic GPSR, and (f) BB GPSR, and the 3D images of the 30th frame, reconstructed by: (g) PCG, (h) basic GPSR, and (i) BB GPSR.

Computational cost. In real-time imaging, e.g., monitoring of pulmonary function, the reconstruction time is vital, which limits the applicability of the 3D reconstruction as a result of the need for a large number of voxels. Table 2 shows the CPU time consumed by the employed solvers for reconstructing 3D images of all the thirty four frames. According to this table, the GPSR noticeably reduced the reconstruction time, compared to the PCG. This table also affirms that the execution of the BB GPSR is more than the basic GPSR. Indeed, the BB scheme does not force the objective function to decrease monotonically through all iterates, and adjusts the step length in a more sophisticated way, so the accuracy of the solution was improved at the cost of the reconstruction time. The results show that the BB and basic GPSR were, respectively, 4.83 and 9.09 times faster than the PCG in reconstructing all the frames.

Table 2. The CPU time elapsed on reconstructing images from the real human lung data over all the thirty four frames (Sec).

PCG	Basic GPSR	BB GPSR
144.79	15.92	29.94

5. Discussion

The results show that both the basic and BB GPSR are more tolerant than the standard sparsity and PCG algorithms for 3D EIT of human chest. To the best of our knowledge, the most valid sparsity solver for EIT is the algorithm proposed in [43], which was then tested on real data in [44,45]. Namely standard sparsity here, we regard this algorithm as the benchmark for testing the performance of the GPSR inverse solvers. According to appendix, the convergence of this algorithm is contingent on computation of a smoothed Sobolev gradient of the residual norm, which imposes some smoothness on the solution, as well as extra time for solving the corresponding Dirichlet boundary

value problem at each iterate. As shown in the simulated results in section 3, the basic and BB GPSR outperformed the standard sparsity solver regarding the accuracy and time.

In addition, the PCG is regarded as the most well-known solver for 3D EIT in both literature and EIDORS website since it does not require the inverse Hessian, in contrast to classical Newton's methods [19, 26-28]. The PCG, however, deleteriously smoothed the solution, and failed to accurately determine sharp conductivity jumps over lung boundary. As a result, the resulting images contain very little information for diagnostic purposes. In addition, although its computational cost is much lower than Newton's method, it is not yet tolerant enough to deal with a large number of finite elements, i.e., more than 20000 voxels. Indeed, the 3D reconstruction for real cases suffers severely from the large number of degrees of freedom of the problem, which increases the ill-posedness, as well as the reconstruction time.

The GPSR was already proposed in the context of signal processing for sparse recovery of signals [31]. A modified version of the GPSR was tailored in this study for the time-difference 3D EIT. Both the numerical and experimental results reveal that the basic and BB GPSR noticeably improved 3D EIT for real-time lung imaging, compared to the PCG and the standard sparsity solvers. Applying the GPSR to the time-difference 3D EIT, the updated conductivity changes with positive and negative values are regarded as separate sparse vectors, and subsequently enforcing a nonnegativity constraint to the gradient projection nulls the background conductivity through the iterates. The results show the high potential of the GPSR for time-difference 3D EIT. The computations only require matrix vector products, so the computational cost arising from explicitly storing $\mathbf{J}$ and $\mathbf{J}^T\mathbf{J}$ will be removed. Both the basic and BB GPSR provided a more accurate conductivity profile during the breathing cycle regarding determination of interfaces, as well as the conductivity amplitude. In addition, the results show that the GPSR better addressed the large number of voxels, and appreciably reduced the CPU time against the competing solvers.

However, according to our previous numerical results, the main drawback of the GPSR for application to 3D EIT is that its accuracy is severely deteriorated in determining very small inclusions [57]. This problem was addressed by adopting a compressive sensing scheme for sampling the finite elements covering the inclusions. By application of a preprocessing PCG step, the proposed scheme improved accuracy at the cost of speed. For further information, the reader is referred to [57].

6. Conclusion

3D EIT typically suffers from the need for a large number of finite elements to cover the whole domain, thus requiring very large computations [26-28]. Although the main advantage of 2D EIT for real-time imaging of lung is its high speed [4,6], the applicability of 3D EIT to this case remains scarce, since the large number of degrees of freedom of the problem increases the computational cost

notably. Indeed, recovery of inter-medium interfaces inside human organs will be erroneous over a coarse mesh. For example, for lung monitoring, sharp jumps over the conductivity profile cannot be detected suitably over a coarse mesh, thus providing misleading physiological information. This study showed that the GPSR algorithm best suits 3D EIT of chest. The GPSR suitably deals with a large number of voxels, and determined the conductivity field more accurately than the PCG and standard sparsity solvers, at the same time considerably reducing the computational time. Further studies are still needed to cope with its poor performance in imaging small-size anomalies.

Appendix

Algorithm 3. The sparsity algorithm proposed for EIT in [43-45] (standard sparsity solver)

Set $\delta\boldsymbol{\sigma}^0 = 0$

While stopping criterion is not satisfied **Do**

$\psi(\delta\boldsymbol{\sigma}^k) = \left\|\delta\mathbf{V} - \mathbf{J}\delta\boldsymbol{\sigma}^k\right\|_2^2$

Compute $\nabla\psi(\delta\boldsymbol{\sigma}^k) = \mathbf{J}^T\left(\mathbf{J}\delta\boldsymbol{\sigma}^k - \delta\mathbf{V}\right)$

Compute the Sobolev smoothed gradient via Dirchlet boundary value problem

$-\kappa\Delta D_s(\delta\boldsymbol{\sigma}^k) + D_s(\delta\boldsymbol{\sigma}^k) = \nabla\psi(\delta\boldsymbol{\sigma}^k)$ in Ω s.t. $D_s(\delta\boldsymbol{\sigma}^k) = 0$ on Γ

Determine the step length α^k via an inner iteration based on the BB scheme

Update the conductivity changes $\delta\boldsymbol{\sigma}^{k+1} = \delta\boldsymbol{\sigma}^k - \alpha^k D_s(\delta\boldsymbol{\sigma}^k)$

$S_\beta(\delta\boldsymbol{\sigma}^{k+1}) = \text{sign}\left(\delta\boldsymbol{\sigma}^{k+1}\right)\ \max\{|\delta\boldsymbol{\sigma}^{k+1}| - \beta, 0\}$

End DO

Where, Ω and Γ represent the medium and its boundary, respectively, and D_s denotes Sobolev smoothed gradient of the residual (See [43]). S_β denotes the soft shrinkage operator with $\beta \propto \alpha^k$, which sets small elements of each update to zero, thus promoting the sparse solution, Δ denotes the Laplacian operator, and κ is a scalar parameter controlling the degree of smoothing of the gradient.

Similar to the GPSR algorithm, the stopping criterion was adopted based on LCP, according to Eqs. (22) and (23) with replacing $\boldsymbol{z}^k$ by $\delta\boldsymbol{\sigma}^k$.

The rationale behind employing the smoothed Sobolev gradient is that heuristically, the direct application of $\nabla\psi$ to this algorithm exhibits unappealing oscillations in the reconstruction, which

often gives rise to numerical instability. This is another superiority of the GPSR over this algorithm, as the GPSR suitably converges through the direct application of the gradient.

Applying the BB scheme, an initial guess for the step length is made according to Eq. (20). This initial guess is then iteratively reduced until the following equation is satisfied

$$\psi\left(\delta\boldsymbol{\sigma}^0 + S_\beta\left(\delta\boldsymbol{\sigma}^k - \alpha^k D_s(\delta\boldsymbol{\sigma}^k)\right)\right) \leq \max_{(k-Q+1\leq i\leq k)} \psi(\delta\boldsymbol{\sigma}^i) - \alpha^k \frac{\mu}{2} \left\| S_\beta\left(\delta\boldsymbol{\sigma}^k - \alpha^k D_s(\delta\boldsymbol{\sigma}^k)\right) - \delta\boldsymbol{\sigma}^k \right\|_2^2, \qquad \text{(A1)}$$

where, i denotes the Q previous iterates, and $\mu \in (0,1)$ is a constant that is often chosen near zero.

Acknowledgment

This work was partially supported by the Federal Ministry of Education and Research (BMBF) in Germany under grant no. 03FH038I3 (MOSES).

References

[1] M. Cheney, D. Isaacson, and J. C. Newell, "Electrical impedance tomography," SIAM Rev., vol. 41, p.p. 85–101, 1999.

[2] D. S. Holder, Electrical Impedance Tomography: methods, history and applications, Institute of Physics Publishing, pp. 3-64, 2004.

[3] A. Adler, J. H. Arnold, R. Bayford, A. Borsic, B. Brown, P. Dixon, T. J. C. Faes, I. Frerichs, H. Gagnon, Y. Gärber, B. Grychtol, G. Hahn, W. R. B. Lionheart, A. Malik, R. P. Patterson, J. Stocks, A. Tizzard, N. Weiler, and G. K. Wolf, "GREIT: a unified approach to 2D linear EIT reconstruction of lung images," Physiol. Meas., vol. 30, No. 6, p.p. 35-55, 2009.

[4] A. Adler, M. B. Amato, J. H. Arnold, R. Bayford, M. Bodenstein, S. H. Böhm, B. H. Brown, I. Frerichs, O. Stenqvist, N. Weiler, and G. K. Wolf, Whither Lung EIT: where are we, where do we want to go and what do we need to get there?," *Physiol. Meas.*, vol. 33, No. 5, p.p. 679-694, 2012.

[5] R. J. Halter, A. Hartov, and K. D. Paulsen, "A broadband high-frequency electrical impedance tomography system for breast imaging," *IEEE Trans. Biomed. Eng.*, vol. 55, No. 2, 2008.

[6] A. P. Bagshaw, A. D. Liston, R. H. Bayford, A. Tizzard, A. P. Gibson, T. Tidswell, M. K. Sparkes, H. Dehghani, C. D. Binnie, and D. S. Holder, "Electrical impedance tomography of human brain function using reconstruction algorithms based on the finite element method," *Neuro Image*, vol. 20, p.p.752-764, 2003.

[7] S. Rezajoo and G. Hossein-Zadeh,"Reconstruction convergence and speed enhancement in electrical impedance tomography for domains with known internal boundaries," *Physiol. Meas.,* vol. 31, p.p. 1499–1516, 2010.

[8] T. J. Yorkey, J. G. Webster, and W. J. Tompkins, "Comparing reconstruction algorithms for electrical impedance tomography," *IEEE Trans. Biomed. Eng.*, vol. 34, p.p. 843–52, 1987.

[9] W. R. B. Lionheart, “EIT reconstruction algorithms: pitfalls, challenges and recent developments,” *Physiol. Meas.*, vol. 25, p.p. 125–42, 2004.

[10] M. Cheney, D. Isaacson, J. C. Newell, S. Simske, and J. Goble, “NOSER: an algorithm for solving the inverse conductivity problem,” *Int. J. Imaging Syst. Technol.*, vol. 2, p.p. 66–75, 1990.

[11] A. Adler and R. Guardo, “Electrical impedance tomography: Regularized imaging and contrast detection ,” *IEEE Trans. Biomed. Eng.*, 15 p.p. 170-9, 1996.

[12] M. Vauhkonen, D. Vadasz, P. A. Karjalainen, E. Somersalo, and J. P. Kaipio, “Tikhonov regularization and prior information in electrical impedance tomography,” *IEEE Trans. Med. Imag.* vol. 17, no.2, p.p. 285-293, 1998.

[13] M. Soleimani, C. Gomez-Laberge, and A. Adler, “Imaging of conductivity changes and electrode movement in EIT,” *Physiol. Meas.*, vol. 27, p.p. 103-113, 2006.

[14] D. C. Barber and B. H. Brown, “Errors in reconstruction of resistivity images using a linear reconstruction technique,” *Clin. Phys. Physiol. Meas.* vol. 9, p.p. 101-104, 1988.

[15] A. Borsic, B. M. Graham, A. Adler, and W. R. B. Lionheart, “*In vivo* impedance imaging with total variation regularization,” *IEEE Trans. Med. Imag.* vol. 29, no. 1, p.p. 44-54, 2010.

[16] A. Javaherian, A. Movafeghi, and R. Faghihi, “Reducing negative effects of quadratic norm regularization on image reconstruction in electrical impedance tomography,” *Appl. Math. Model.*, vol. 37, no. 8, p.p. 5637–5652, 2013.

[17] A. Borsic, W. R. B. Lionheart, and C. N. McLeod, “Generation of anisotropic-smoothness regularization filters for EIT,” *IEEE Trans. Med. Imag.* vol. 21, no. 6, p.p. 579-587, 2002.

[18] D. C. Dobson and F. Santosa, “An image enhancement technique for electrical impedance tomography,” *Inv. Probl.*, vol. 10, pp. 317–334, 1994.

[19] Electrical Impedance Tomography and Diffuse Optical Tomography Reconstruction Software (EIDORS), Released version: EIDORS 3.7.1 (29 May 2013), http://eidors3d.sourceforge.net/

[20] B. M. Graham and A. Adler, “Electrode placement configurations for 3D EIT,” *Physiol. Meas.* vol. 28, p.p. 29–44, 2007.

[21] J. C. Gobel, M. Cheney, and D. Isaacson, “Electrical Impedance Tomography in three dimensions,” *Appl. Comput. Electromagn. Soc. J.* vol. 7, p.p. 128-147, 1992.

[22] P. Metherall, D. C. Barber, R. H. Smallwood, and B. H. Brown, “Three dimensional electrical impedance tomography,” *Nature*, vol. 380, p.p. 509-512, 1996.

[23] P. J. Vauhkonen, M. Vauhkonen, T. Savolainen, and J. P. Kaipio, “Three dimensional electrical impedance tomography based on the complete electrode model,” *IEEE Trans. Biomed. Eng.* Vol. 46, p.p. 1150-1160, 1999.

[24] R. J. Halter, A. Hartov, and K. D. Paulsen, “Experimental justification for using 3D conductivity reconstructions in electrical impedance tomography,” *Physiol. Meas.* vol. 28, p.p. 115–127, 2007.

[25] M. Goharian, M. Soleimani, and G. Moran, "A trust region subproblem for 3D electrical impedance tomography inverse problem using experimental data," *Progress Electromagnetics Research-PIER*, vol. 94, p.p. 19-32, 2009.

[26] C. L. Yang, H. Y. Wei, A. Adler, and M. Soleimani, "Reducing computational costs in large scale 3D EIT by using a sparse Jacobian matrix with block-wise CGLS reconstruction," *Physiol. Meas.* vol. 34, p.p. 645–658, 2013.

[27] A. Javaherian and M. Soleimani, "Compressed sampling for boundary measurements in three-dimensional electrical impedance tomography," *Physiol. Meas.* vol. 34, p.p.1133-50, 2013.

[28] L. Horesh, M. Bolhofer, M. Schweiger, S. R. Arridge, and D. S. Holder, "Novel large-scale 3D electrical impedance tomography modeling of the human head," *IFMBE Proceedings*, vol. 14, p.p. 3858-3861, 2007.

[29] R. S. Blue, D. Isaacson, and J. C. Newell, "Real-time three-dimensional electrical impedance imaging," *Physiol Meas.*, vol. 21, p.p. 1-12, 2000.

[30] W. R. Fan and H. X. Wang, 3D modeling of the human thorax for ventilation distribution measured through electrical impedance tomography, *Meas. Sci. Technol.*, vol. 21**,** 115801 (8pp), 2010.

[31] M. Figueiredo, R. Nowak, and S. Wright, "Gradient projection for sparse reconstruction: application to compressed sensing and other inverse problems," *IEEE Journal of selected topics in signal processing*, vol. 1, p.p. 586-98, 2007.

[32] S. J. Kim, K. Koh, M. Lustig, S. Boyd, and D. Gorinevsky, "An interior-point method for large-scale ℓ_1-regularized least squares," *IEEE Journal of Selected Topics in Signal Processing*, vol. 1, no. 4, p.p. 606-617, 2007.

[33] J. Bioucas-Dias and M. Figueiredo, "A new TwIST: Two-step iterative shrinkage/thresholding algorithms for image restoration," *IEEE Trans. Image Process.*, vol. 16, no. 12, pp. 2992–3004, Dec. 2007.

[34] T. Hale, W. Yin and Y. Zhang, "A fixed-point continuation method for ℓ_1-regularized minimization with applications to compressed sensing," Dept. Computat. Appl. Math., Rice Univ., Houston, TX, Tech. Rep.TR07-07, 2007.

[35] X. He, J. Liang, X. Wang, J. Yu, X. Qu, X. Wang, Y. Hou, D. Chen, F. Liu, and J. Tian "Sparse reconstruction for quantitative bioluminescence tomography based on the incomplete variables truncated conjugate gradient method," *Optics Express,* vol. 18, no. 24, pp. 24825-24841, 2010.

[36] Y. Yu, M. Hong, F. Liu, H. Wang and S. Crozier, "Comparison and analysis of nonlinear algorithms for compressed sensing in MRI," *32nd Annual International Conference of the IEEE EMBS*, Buenos Aires, Argentina, September 2010.

[37] D. Thompson, Z. Harmany and R. Marciat, "Sparse Video Recovery using linearly Constrained Gradient projection," *IEEE International Conference on Acoustic, Speech and Signal Processing (ICASSP)*, Prague, Czech, 22-27 May, 2011.

[38] J.C. park, B. Song, J. S. Kim, S. H. Park, H. K. Kim, Z. Liu, T. S. Suh and W. Y. Song, "Fast compressed sensing-based CBCT reconstruction using Barzilai-Borwein formulation for application to on-line IGRT," *Med. Phys.* Vol. 39, no. 3, pp. 1207-1217, 2012.

[39] G.A. Howland, D. J. Lum and J. C. Howell, "Compressive wavefront sensing with weak values," *optics Express*, vol. 22, no.16, pp. 18870-18880, 2014.

[40] X. Xu, E. Li, H. Yu, W. Gong and S. Han, "Morphology separation in ghost imaging via sparsity constraint,", *Optics Express,* vol. 22, no. 12, pp. 14375-14381, 2014.

[41] A. P. Cuadros, G. R. Arce and H. Arguello, "Coded aperture design in compressive x-ray tomography," *IEEE Global Conference on Signal and Information Processing*, 3-5 December, 2014.

[42] D. Brunelli and C. Caione, "Sparse recovery optimization in wireless sensor networks with a sub-Nyquist sampling rate," *Sensors,* vol. 15, pp. 16654-16673, 2015.

[43] B. Jin, T. Khan and P. Maass, "A reconstruction algorithm for electrical impedance tomography based on sparsity regularization," *Int. J. Numer. Meth. Engng.* vol. 89, pp. 337–353, 2012.

[44] M. Gehre, T. Kluth, A. Lipponen, B. Jin, A. Seppänen, J. P. Kaipio and P. Maass, "Sparsity reconstruction in electrical impedance tomography: An experimental evaluation," *J. Comput. Appl. Math.,* vol. 236, pp. 2126–2136, 2012.

[45] M. Gehre, T. Kluth, C. Sebu and P. Maass, "Sparse 3D reconstructions in electrical impedance tomography using real data," *Inverse Probl. Sci. En.,* vol. 22, no. 1, pp. 31-44, 2014.

[46] Y. Mamatjan, A. Borsic, D. Gursoy and Andy Adler, "An experimental clinical evaluation of EIT imaging with ℓ_1 data and image norms," *Physiol. Meas.* 34 (2013) 1027–1039.

[47] J. R. Shewchuk, An introduction to the conjugate gradient method without the agonizing pain, Carnegie Mellon University, Pittsburgh, USA, 1994.

[48] R. Tibshirani, "Regression shrinkage and selection via the lasso," *J. R. Statist. Soc. B*, vol. 58, pp. 267–288, 1996.

[49] S. Chen, D. Donoho, and M. Saunders, "Atomic decomposition by basis pursuit," *SIAM J. Sci. Comput.*, vol. 20, pp. 33–61, 1998.

[50] D. P. Bertsekas*, Nonlinear Programming*, 2nd ed. Boston, MA: Athena, 1999.

[51] S. J. Wright, R. D. Nowak, and M. A. T. Figueiredo, "Sparse reconstruction by separable approximation," *IEEE Trans. Signal Process.,* vol. 57, pp. 2479–2493, 2009.

[52] J. Barzilai and J. Borwein, "Two point step size gradient methods," *IMA J. Numer. Anal.*, vol. 8, pp. 141–148, 1988.

[53] B. Xiao and P. T. Harker, "Perturbation results for the linear complementarity problem," *Applied Mathematics Letters*, vol. 2, no. 4, pp. 401-405, 1989.

[54] Gradient Projection for Sparse Reconstruction (GPSR v6.0), www.lx.it.pt/~mtf/GPSR/

[55] Netgen Mesh Generator (v5.0), http://sourceforge.net/projects/netgen-mesher/files/netgen-mesher/5.0/

[56] Electrical Impedance Tomography and Diffuse Optical Tomography Reconstruction Software (EIDORS), http://eidors3d.sourceforge.net/tutorial/lung_EIT/tutorial310-lung-images.shtml

[57] A. Javaherian, M. Soleimani and K. Moeller, "Sampling of finite elements for sparse recovery in large scale 3D electrical impedance tomography," *Physiol. Meas.,* vol. 36, no.1**,** pp. 43–66, 2015.

Author's Biography:

Ashkan Javherian received a B.Sc. in Biomedical Engineering, majoring in Bioelectric, and an M.Sc. in Medical Radiation Engineering from Shiraz University, Iran, in 2007 and 2010, respectively. From 2010 to 2013, he worked as a collaborative researcher with School of Mechanical Engineering, Shiraz University, Iran. Since 2013, he has worked as a junior scientist in Institute of Technical Medicine (ITEM), Faculty of Medical and Life Sciences, Furtwangen University of Applied Sciences, Germany. His research interest is mathematics of non-ionising imaging modalities. He has also worked in industry on software and electronics of medical imaging systems.

Manuchehr Soleimani received B.Sc. degree in electrical engineering and the M.Sc. degree in biomedical engineering, and the Ph.D. degree in inverse problems and electromagnetic tomography from the University of Manchester, Manchester, U.K., in 2005. From 2005 to

2007, he was a Research Associate with the School of Materials, University of Manchester. In 2007, he joined the Department of Electronic and Electrical Engineering, University of Bath, Bath, U.K., where he was a Research Associate and he then became a Lecturer in 2008, Senior Lecturer in 2013 and Reader in 2015. He has authored/co-authored over 100 journal papers, and holds several patents. In 2011, he found the Engineering Tomography Laboratory (ETL) at the University of Bath, working in tomographic imaging.

K. Möller received a M.S. and a Ph.D. degree in computer science, and a M.D. in medice from the University of Bonn, Bonn, Germany, in 1986, 1991, and 1996, respectively.

From 1991 to 1997, he was an Assistant Professor in the Department of Computer Science, Bonn University, Bonn, Germany, where he was involved in the fields of machine learning, robotics, and image processing. In 1998, he became a Professor of Medical Informatics at Furtwangen University, Villingen-Schwenningen, Germany, where he currently is Director of the Institute of Technical Medicine (ITeM) and the Head of the Biomedical Engineering Division. His research interests include decision support systems, modeling, and signal analysis with the application to lung protective mechanical ventilation.

Prof. Möller is a member of the German Society of Biomedical Engineering (DGBMT) and of the German Association for Electrical, Electronic & Information Technologies (VDE).